Photodetection properties of populated Fe$_3$O$_4$@TiO$_2$ core–shell/Si heterojunction prepared by laser ablation in water

Hasan H. Bahjat[1] · Raid A. Ismail[1] · Ghassan M. Sulaiman[1]

Abstract

In this work, we demonstrated the first study on the preparation and characterization of the populated Fe$_3$O$_4$@TiO$_2$ core–shell/Si photodetector by laser ablation in liquid. The structural and optical properties of Fe$_3$O$_4$ nanoparticles and Fe$_3$O$_4$@TiO$_2$ core–shell nanoparticles were studied by X-ray diffraction, transmission electron microscope, and UV–Vis absorption. X-ray diffraction findings suggest the formation of a populated crystalline Fe$_3$O$_4$@TiO$_2$ core–shell through the existence of XRD peaks related to TiO$_2$ and Fe$_3$O$_4$. The optical properties revealed that the optical energy gap of Fe$_3$O$_4$@TiO$_2$ was 3 eV, while the optical energy gap of Fe$_3$O$_4$ was 2.8 eV. Raman studies reveal the presence of vibration modes centered at 91 cm^{-1} (E_g), 144 cm^{-1} (E_g), 396 cm^{-1} (B_{1g}), 512 cm^{-1} (B_{1g}), 541 cm^{-1} ($B_{1g}+A_{1g}$), and 609 cm^{-1} (E_g) which are belong to the TiO$_2$. The vibration modes related to the magnetite Fe$_3$O$_4$ are observed at 145^{-1} (T_{2g}), 302 cm^{-1} (T_{2g}), and 554 cm^{-1} (T_{1g}). Transmission electron microscope results suggest the presence of a core–shell morphology with an average size of 60 nm. The current–voltage characteristics of Fe$_3$O$_4$/p-Si and Fe$_3$O$_4$@TiO$_2$ core–shell/p-Si photodetectors are measured in the dark and under illumination conditions. The maximum responsivity of the Fe$_3$O$_4$@TiO$_2$/Si photodetector was 0.5A/W at 400 nm, while the maximum responsivity of Fe$_3$O$_4$/p-Si photodetector was 0.4A/W at 500 nm. The specific detectivity and external quantum efficiency of the Fe$_3$O$_4$@TiO$_2$/p-Si photodetector are larger than those of Fe$_3$O$_4$/p-Si photodetector.

Keywords Core–shell · Fe$_3$O$_4$@TiO$_2$ · Laser ablation · Photodetector

1 Introduction

Nanomaterials have drawn attention due to their unique optical and electrical characteristics compared to those of the bulk state [1]. These materials are considered promising and efficient for a variety of industrial and technological applications, for example, renewable power converters, sensing applications, corrosion resistance, catalysts, solar cells, photodetectors, and chemical and biochemical sensors [2–6]. The core–shell structure is a nanoparticle core covered by a certain thin layer of semiconducting material (shell) in order to decrease the reactivity and improve the dispersibility of the core nanoparticles. Additionally, the shell layer can supply surface chemistry for further modification and functionalization of the core nanoparticles. The core–shell structure was used for photodetectors to improve the performance of

the photodetector figures of merit and manipulate the peak response. High-performance Ag@PbS-based core–shell photodetector, Ag@PbI$_2$/Si, and Au@CuO/Si core–shell structure photodetector have been reported [7–10]. The Fe$_3$O$_4$@TiO$_2$ core–shell structure is promising, and it has been subjected to extensive studies. Due to their tunable magnetic properties, iron oxide (Fe$_3$O$_4$) nanoparticles are very attractive materials. Titanium dioxide (TiO$_2$) nanoparticles have been used in the synthesis of core–shell structures as a photocatalytic agent. As reported, the Fe$_3$O$_4$@TiO$_2$ core–shell structure is stable, environmentally friendly, and biocompatible, and by controlling the core diameter and shell thickness; it can be used for important applications [11]. Fe$_3$O$_4$@TiO$_2$ core–shell structures have been used for many potential biomedical and biochemical applications [12, 13]. Pulsed laser ablation in liquid (PLAL) is a process in which the target is immersed in liquid and irradiated with high intensity laser pulses that result in the production of colloidal nanoparticles. PLAL exhibits many advantages, such as stability, inexpensive, simplicity, attractive size distribution, different particle morphologies, and does not need

✉ Raid A. Ismail
raidismail@yahoo.com

1 Department of Applied Sciences, University of Technology, Baghdad, Iraq

a vacuum [14–18]. Herein, a novel route to the synthesis of $Fe_3O_4@TiO_2$ core–shell structures was demonstrated. The PLAL technique was used to fabricate $Fe_3O_4@TiO_2$/Si photodetector. The optoelectronic properties of the $Fe_3O_4@TiO_2$ core–shell/Si photodetector were measured and compared with those of Fe_3O_4 NPs/Si photodetector.

2 Experimental work

To synthesize $Fe_3O_4@TiO_2$ core–shell nanoparticles, Fe_3O_4 NPs were synthesized first by laser ablation of a high purity Fe_3O_4 pressed pellet (supplied by Alfa Aesar company) immersed in deionized water (DI). The Fe_3O_4 pellet was sintered at 1000 °C using a tube furnace. For ablation of iron oxide nanoparticles, a pulsed Nd: YAG laser with a wavelength of 1064 nm, pulse width of 7 ns, and laser fluence of 20 mJ/cm^2/pulse was used. In the second step, a high purity TiO_2 powder (99.9%) (a mix of anatase and rutile tetragonal) purchased from BDH was pressed to prepare a pellet and then positioned inside the glass vessel filled with colloidal Fe_3O_4 nanoparticles and then irradiated with the same Nd:YAG laser with a laser fluence of 30 mJ/cm^2/pulse. The focusing of the laser beam on the Fe_3O_4 and TiO_2 targets was performed using a converging lens with a focal length of 10 cm. The effective laser spot size was around 0.6 mm on the Fe_3O_4 and 0.7 mm on the TiO_2 target. Figure 1 shows the schematic diagram of the PLAL system used for the synthesis of $Fe_3O_4@TiO_2$ core–shell nanoparticles. The ablation time was adjusted to be 30 min for each step of ablation. The structures of Fe_3O_4 NPs and $Fe_3O_4@TiO_2$ core–shell NPs were studied using an X-ray diffractometer (XRD-6000, Shimadzu). The size and morphology of the nanoparticles were investigated using transmission electron microscopy TEM (EM208, Philips). An energy dispersive X-ray EDX equipped with a scanning electron microscope FE-SEM (Arya Electron Optic) was utilized to estimate the chemical composition of $Fe_3O_4@TiO_2$. The optical absorbance of the colloidal nanoparticles was measured using a spectrophotometer (Metertech, SP8001 Japan).

To construct the photodetectors, a thin layer of Fe_3O_4 NPs and $Fe_3O_4@TiO_2$ core–shell NPs were deposited on mirror-like silicon substrates separately by the drop casting technique. The silicon substrate used was p-type with an orientation of (100) and had an electrical resistivity of 1–3 Ωcm. Cleaning the substrate was accomplished by the standard route. After the deposition, indium and aluminum were deposited on $Fe_3O_4@TiO_2$ and the backside of the silicon substrate, respectively, as ohmic contacts through a square mask of 1cm^2 area using a thermal evaporation system. The current–voltage characteristics of Fe_3O_4/Si and $Fe_3O_4@TiO_2$/Si heterojunction photodetectors were measured under dark ad illumination at room temperature. To investigate the spectral responsivity of the photodetectors, a monochromator (Jobin Yvon) was used in the spectral range of 350–800 nm after power calibration using a silicon power meter.

Fig. 1 Schematic illustration of laser ablation of $Fe_3O_4@TiO_2$ core–shell NPs experimental setup
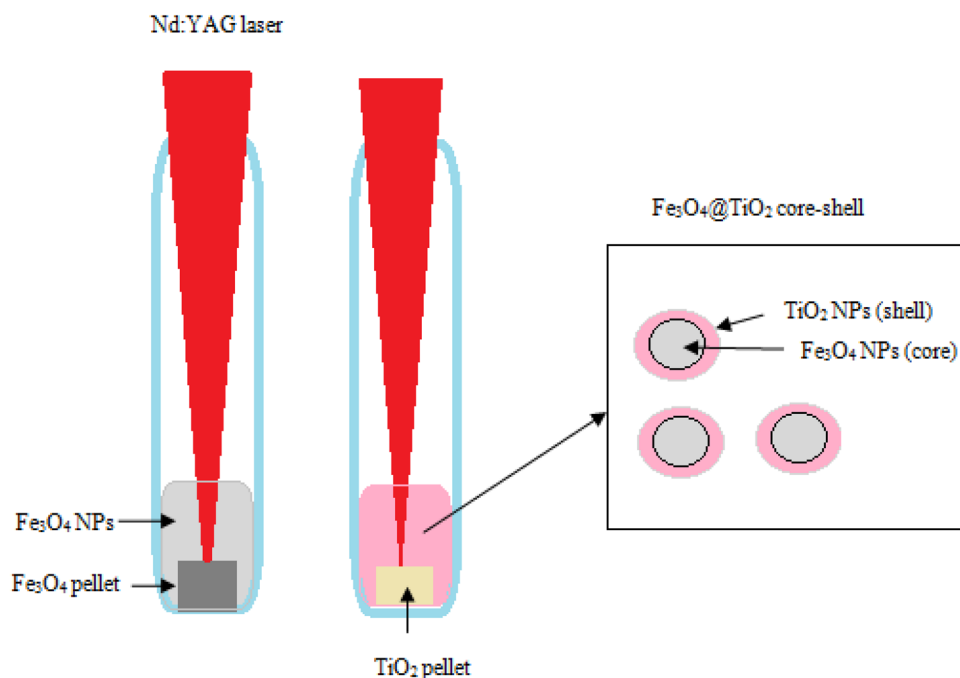
3 Results and discussion

The XRD patterns of TiO_2, Fe_3O_4, and Fe_3O_4@TiO_2 nanoparticles are shown in Fig. 2. Eight peaks for Fe_3O_4 located at $2\theta = 17.5°$, $28.4°$, $30.1°$, $33.4°$, $35.3°$, $43.3°$, $54.7°$, $62.1°$, and $68.2°$ corresponding to (111), (220), (102), (311), (222), (004), (224), (440), and (044) planes, respectively, were observed which were indexed to the cubic magnetite [19]. Some XRD peaks related to the Fe_2O_3 nanoparticles were also detected, which agrees with reported data [20]. The XRD pattern of TiO_2 powder confirmed the observed peaks belong to the tetragonal anatase phase (denoted by A) and rutile phase (denoted by R) TiO_2 according to JCPDs # 21–1272 and # 21–1276, respectively. As we can see, the XRD pattern of Fe_3O_4@TiO_2 core–shell nanoparticles exhibited eleven peaks. Four of them are located at $2\theta = 25.8°$, $27.4°$, $40.3°$, and $54.3°$ corresponding to (110), (100), (112), and (211) plane, respectively, which belong to TiO_2 NPs and the other peaks are indexed to Fe_3O_4 NPs [21]. Table 1 lists the crystallite size of Fe_3O_4 NPs and Fe_3O_4@TiO_2 nanoparticles for two dominant planes.

The appearance of XRD peaks of Fe_2O_3 can be ascribed as follows: The repeating ablating of the target and creating fresh O atoms disrupts the O_2 partial pressure balance in the laser plume. When the partial pressure of oxygen in the plume changes, different iron oxides, such as Fe_2O_3, develop. Figure 3-a shows the optical absorption spectra of colloidal Fe_3O_4 and Fe_3O_4@TiO_2 core–shell NPs. The absorption in the UV region of Fe_3O_4@TiO_2 is higher than that of Fe_3O_4 due to the presence of a nanocomposite structure consisting of TiO_2 and Fe_3O_4. The absorption decreases sharply after 200 nm and saturates after 400 nm for two samples. A small absorption peak was observed at 250 nm due to the quantum size effect of nanosized Fe_3O_4 and Fe_3O_4@TiO_2 comes from the high energy of exciton. The freshly prepared colloidal Fe_3O_4 and Fe_3O_4@TiO_2 core–shell suspension is shown in the inset of Fig. 3-a. It is clear that the color of the colloidal nanoparticles was changed after ablation, from transparent

Table 1 XRD analysis of Fe_3O_4 NPs and Fe_3O_4@TiO_2 core–shell NPs

Sample	2Θ(degree)	Peak position [°2Th]	FWHM	Crystallite size (nm)
Fe_3O_4	0.248	54.2	0.24	37
	0.207	37.2	0.199	42
Fe_3O_4@TiO_2	0.165	28.265	0.157	52
	0.496	22.014	0.488	16
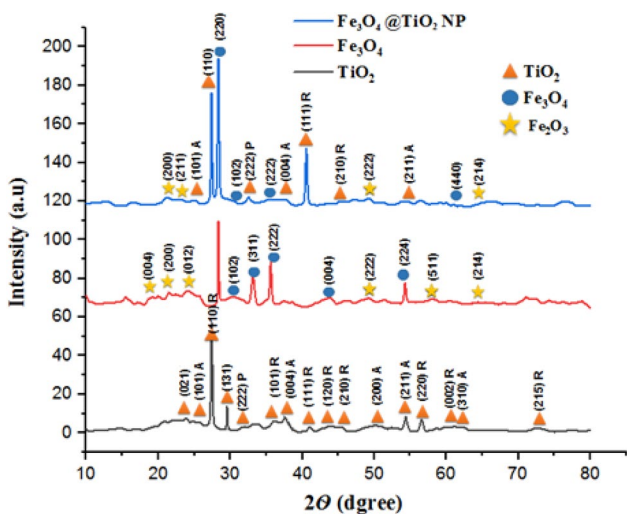
Fig. 2 XRD patterns of Fe_3O_4, TiO_2, and populated Fe_3O_4@TiO_2 core–shell NPs
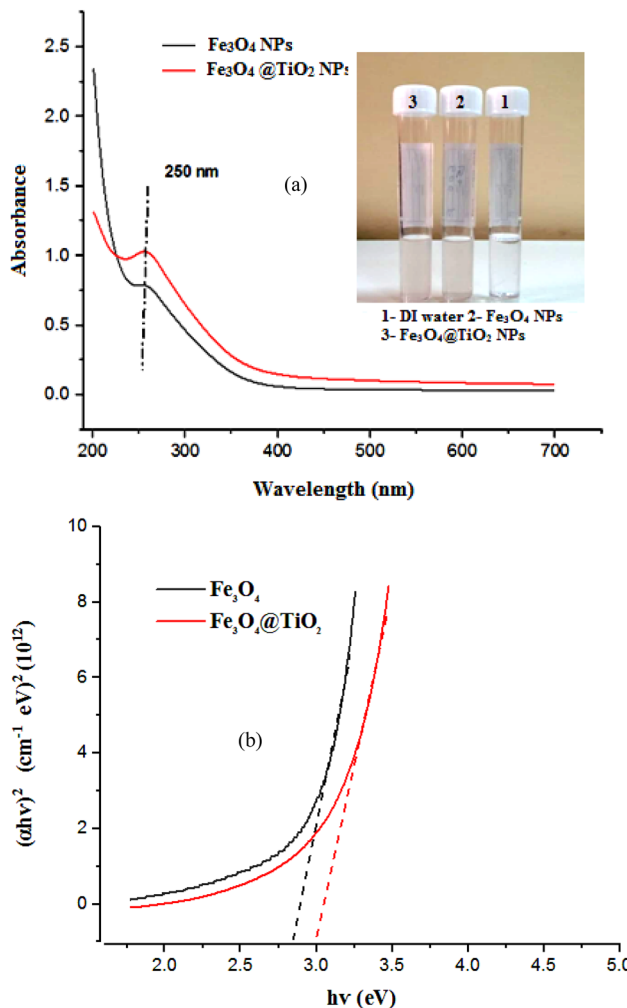
Fig. 3 a Optical absorption of Fe_3O_4 NPs and Fe_3O_4@TiO_2 core–shell NPs. Inset is the photograph colloids and (b) is $(\alpha h\nu)^2$ versus photon energy plot

to light pink. It is obvious that the color of the colloidal is mostly dependent upon the size and concentration of the nanoparticles in colloids. As shown in Fig. 3-b, the optical energy gap of the nanoparticles was determined from Tauc plot via plotting $(\alpha h\nu)^2$ (α is absorption coefficient) against photon energy ($h\nu$) and extrapolation of the linear part to the x-axis gives the energy gap [22, 23]. The optical energy gap of Fe_3O_4 and $Fe_3O_4@TiO_2$ NPs was 2.8 and 3 eV, respectively, as shown in Fig. 3-b. The energy gap of the Fe_3O_4 increased after core–shell formation, indicating the presence of $Fe_3O_4@TiO_2$ core–shell structure.

The TEM images of Fe_3O_4 and $Fe_3O_4@TiO_2$ core–shell NPs are shown in Fig. 4. The TEM image of Fe_3O_4 shows the formation of small, aggregated, and agglomerated spherical nanoparticles due to the high surface energy and van der Waals attraction force [24, 25].

The formation of particles of different sizes can be attributed as follows: The small particles produced inside the laser-induced plasma try to escape from the laser plume into liquid media and are cooled without any grain growth. While the particles remain inside the plasma, they grow and form large particles due to the high temperature [26]. The average particle size of Fe_3O_4 and populated $Fe_3O_4@TiO_2$ was determined using Image J software and found to be 22 nm and 60 nm, respectively. The TEM image shown in Fig. 4-b suggests the presence of the populated core–shell and free nanoparticles. Figure 4-c shows a TEM image of a mono-dispersed core–shell, it revealed that the TiO_2 shell surrounds several Fe_3O_4 cores nanoparticles. As shown in Fig. 4, not all the synthesized nanoparticles have a core–shell morphology, and the estimation of the yield of core–shell production is very important for device application, and this needs deep study and new characterization [27, 28]. Figure 5 shows the EDX spectra of Fe_3O_4 and populated $Fe_3O_4@TiO_2$ core–shell NPs.

The EDX spectrum of Fe_3O_4 NPs showed the presence of only iron and oxygen elements, while the EDX spectrum of $Fe_3O_4@TiO_2$ core–shell NPs reveals the existence of iron, oxygen, and titanium elements. The origin of the Ti element comes from the presence of TiO_2 NPs in solution and from the shell, depending on the core–shell production yield. Figure 6 shows Raman spectra of Fe_3O_4 NPs and $Fe_3O_4@$

Fig. 4 **a** TEM image of Fe_3O_4 NPs, **b** TEM image $Fe_3O_4@TiO_2$ core–shell NPs. and **c** TEM image of mono-dispersed core–shell structure
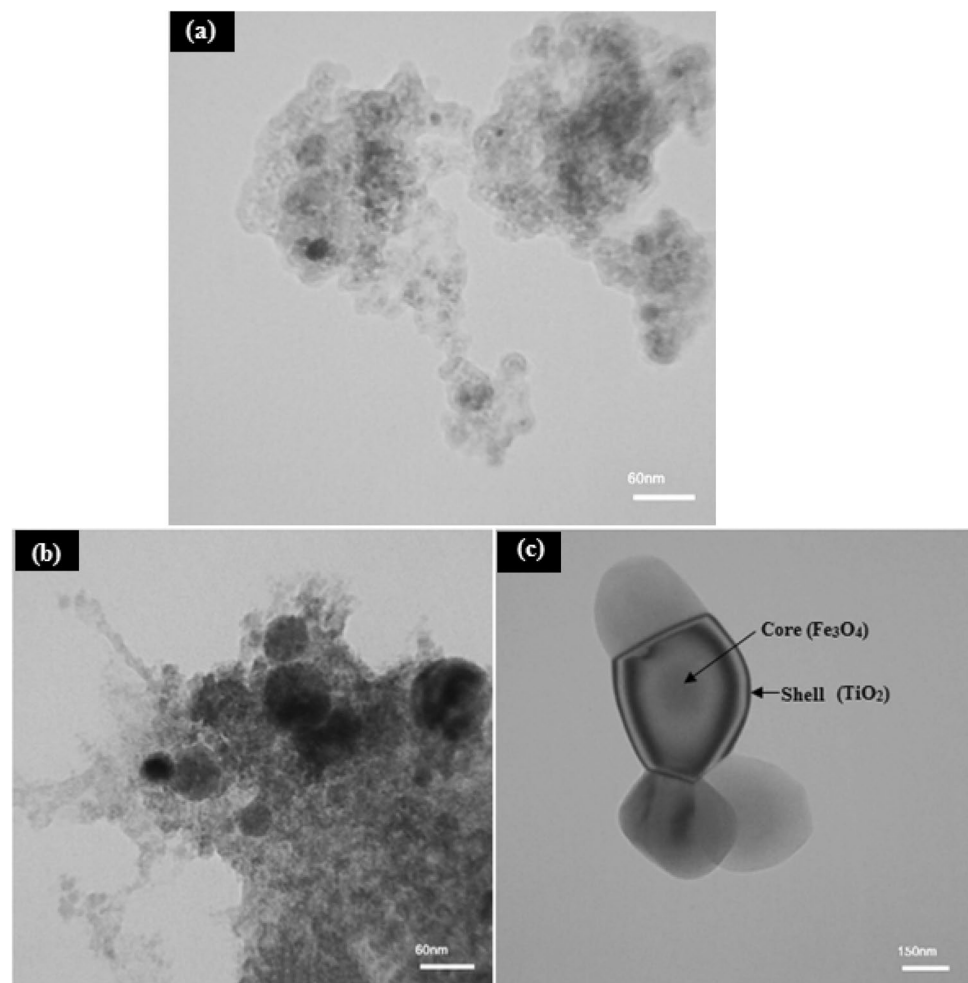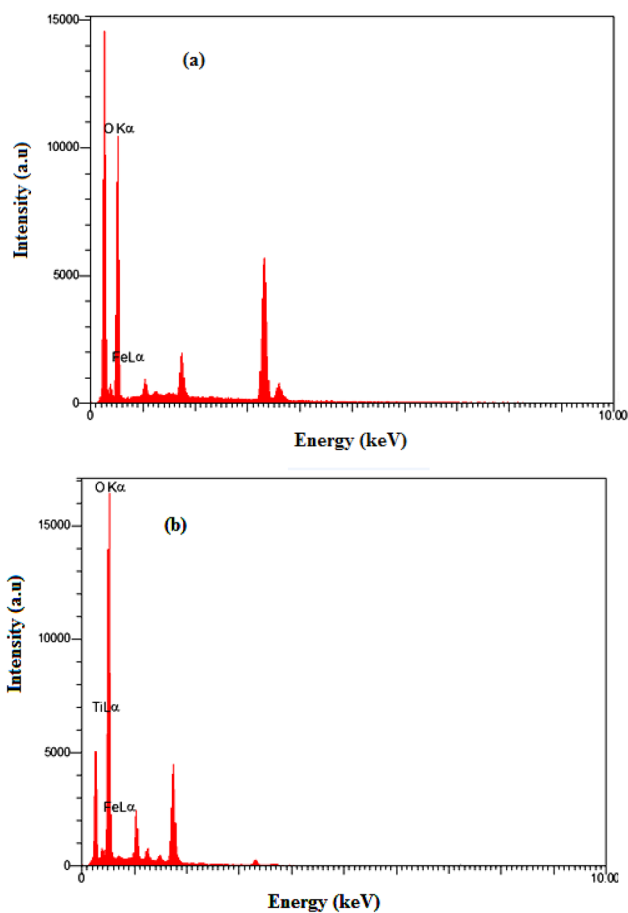
Fig. 5 **a** EDX spectrum of Fe₃O₄ NPs and **b** EDX spectrum of Fe₃O₄@TiO₂ core- shell NPs
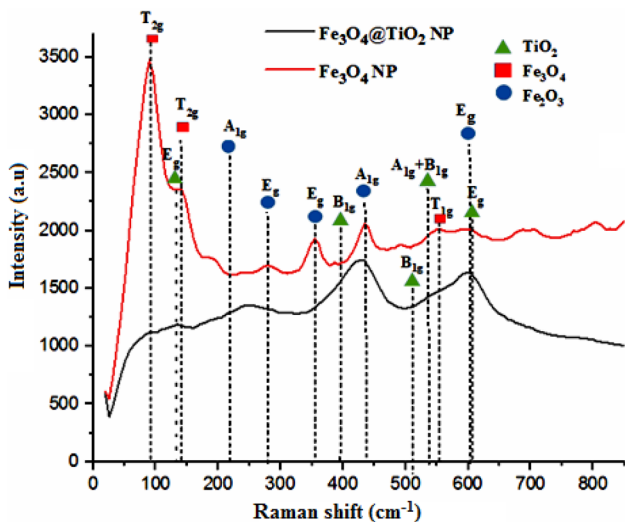
Fig. 6 Raman spectra of Fe₃O₄ NPs and Fe₃O₄@TiO₂ core–shell NPs

TiO₂ core–shell NPs. The Raman spectra of populated Fe₃O₄@TiO₂ NPs showed the vibration modes centered at 144 cm^{-1} (E_g), 396 cm^{-1} (B_{1g}), 512 cm^{-1} (B_{1g}), 541 cm^{-1} ($B_{1g}+A_{1g}$), and 609 cm^{-1} (E_g). These vibration modes are indexed to the anatase and rutile phases of TiO₂, which is in good agreement with the results of XRD. Three vibration modes belonging to magnetite Fe₃O₄ were observed at 94 cm^{-1} (T_{2g}), 145^{-1} (T_{2g}) and 554 cm^{-1} (T_{1g}). Furthermore, Raman peaks related to the Fe₂O₃ phase are also observed in Fig. 6 [26, 29–31].

Figure 7 shows the dark and illuminated I-V characteristics of Fe₃O₄/Si and populated Fe₃O₄@TiO₂/Si heterojunction photodetectors measured at room temperature. The photodetectors exhibit rectification behavior, indicating the formation of a junction between the Fe₃O₄@TiO₂ layer and the silicon substrate. The forward current increases as the bias voltage increases due to the decrease in the depletion layer width [32], and the turn-on voltage of the Fe₃O₄/Si and Fe₃O₄@TiO₂/Si heterojunctions was 1.3 and 1 V, respectively. The forward current of the Fe₃O₄@TiO₂/Si photodetector is larger than that of the Fe₃O₄/Si due to the decrease in the electrical resistivity of Fe₃O₄ after making a nanocomposite with TiO₂ NPs.

The reverse current of the two heterojunctions was slightly increased with reverse bias voltage and no breakdown was observed up to a bias voltage of 5 V. By using the following diode equation, the ideality factor (β) of the heterojunction was calculated by

$$\beta = \frac{q\Delta V}{kT\ln\frac{\Delta I}{I_s}} \tag{1}$$

where I_s is the saturation current, which is determined from the semi-logarithmic I_f-V plot (inset of Fig. 7), k is the Boltzman coefficient, and T is the operating temperature. The value of β for Fe₃O₄/Si and Fe₃O₄@TiO₂ core–shell/Si heterojunctions were 7 and 3.5, respectively, indicating the presence of structural defects [33, 34]. The reverse current of the photodetector was increased after being illuminated with white light due to the generation of e–h pairs as a result of photon absorption in the sensitive area. The photocurrent of the Fe₃O₄@TiO₂ core–shell/Si is larger than that of Fe₃O₄ / Si by a factor of 1.6 at a bias voltage of 5 V and a light intensity of 30mW/cm² due to the increase in the light absorption as well as the decrease in the structural defects [35, 36]. On the other hand, the TiO₂ NPs act as a buffer layer that contributes to the reduction in the lattice constant mismatch between the Fe₃O₄ and the silicon substrate. As we can see from Fig. 7, increasing the light intensity causes an increase in the photocurrent of the photodetector as a result of the production of more e–h pairs in the depletion region. No saturation in the photocurrent was noticed after increasing the light intensity to 30mW/cm². This result indicates that

Fig. 7 Dark and illuminated I-V characteristics of **a** populated Fe$_3$O$_4$ NPs/Si photodetector and **b** Fe$_3$O$_4$@TiO$_2$ core–shell NPs/Si photodetector. The upper inset is the semi-logarithmic relationship of ln I$_f$-Vs and lower inset is the cross sectional view of Fe$_3$O$_4$@TiO$_2$ core–shell NPs/Si photodetector
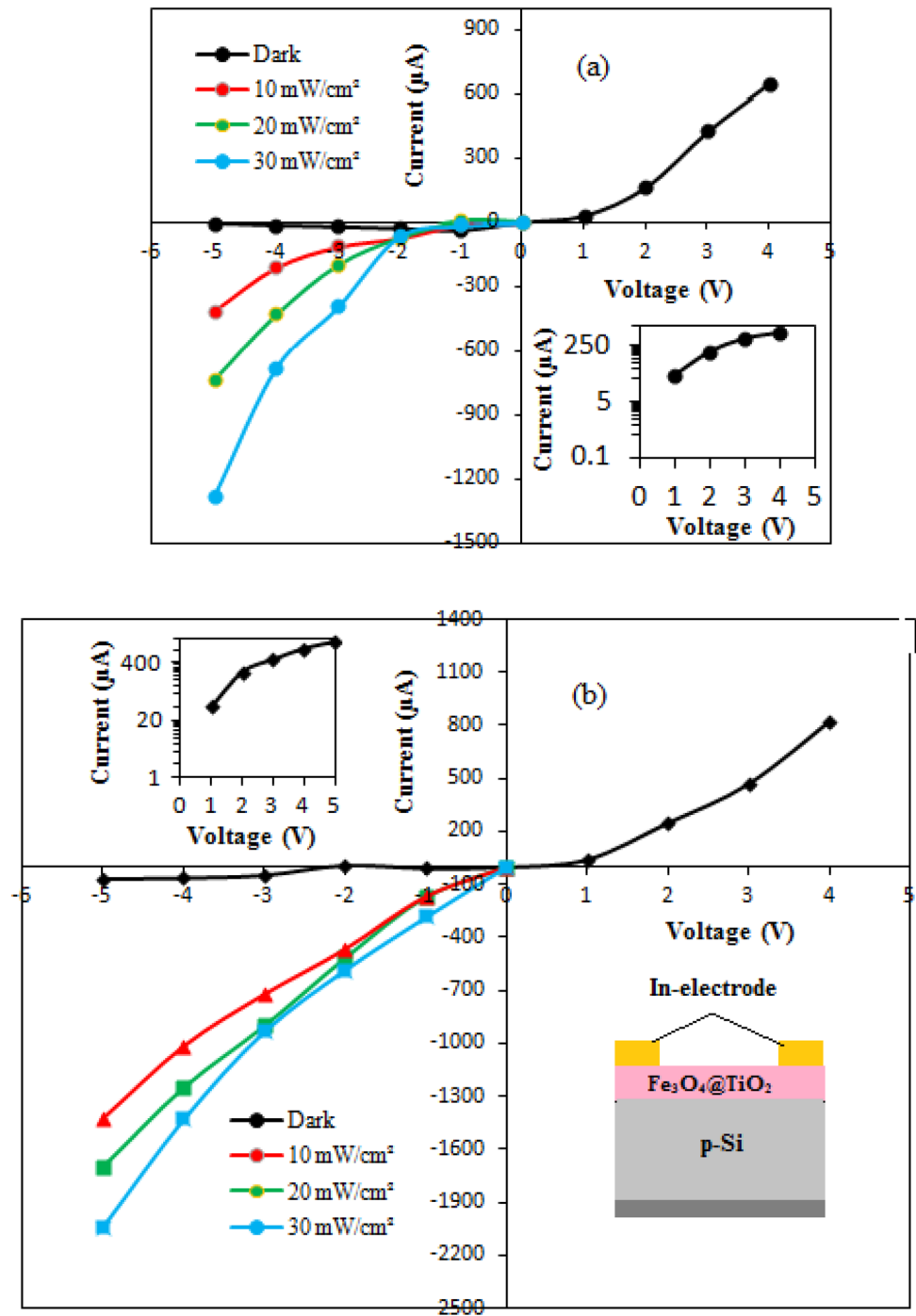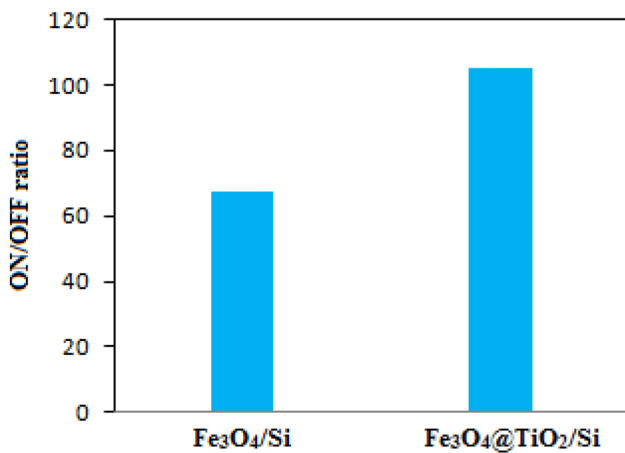
the fabricated photodetectors have good linearity characteristics. The ON/OFF ratio is estimated as shown in Fig. 8, and it was found to be 65.5 and 105 for Fe$_3$O$_4$/Si and Fe$_3$O$_4$@TiO$_2$ core–shell/Si photodetectors, respectively. This result indicates that the presence of the TiO$_2$ shell significantly improved the photodetection ability and figures of merit of the Fe$_3$O$_4$/Si photodetector.

The responsivity R_λ of the photodetector was determined using the following equation:

$$R_\lambda = \frac{I_{ph}}{P} \tag{2}$$

where I_{ph} is the photocurrent and P is the power of light at a certain wavelength. The variation of the responsivity with wavelength for the Fe$_3$O$_4$/Si and Fe$_3$O$_4$@TiO$_2$ core–shell/Si photodetectors at a bias voltage of 5 V is shown in Fig. 9. The responsivity plot of Fe$_3$O$_4$@TiO$_2$ core–shell /Si showed the presence of a peak response at 400 nm with

Fig. 8 ON/OFF ratio of Fe$_3$O$_4$/Si and Fe$_3$O$_4$@TiO$_2$ core–shell/Si photodetectors

Fig. 9 Spectral responsivity plots of Fe$_3$O$_4$NPs/Si photodetector and Fe$_3$O$_4$@TiO$_2$ core–shell NPs/Si photodetectors at 5 V bias

Table 2 D* and NEP of the photodetectors

Photodetector	D* (Jones)	NEP (pW)
Fe$_3$O$_4$/Si	1.3×10^{11}	7.6
Fe$_3$O$_4$@TiO$_2$/Si	1.9×10^{11}	5.2

Fe$_3$O$_4$/Si and Fe$_3$O$_4$@TiO$_2$/Si photodetectors. The specific detectivity of the photodetector can be estimated by

$$D^* = \frac{I_{\mathrm{ph}}(A)^{1/2}}{P(2eI_{\mathrm{d}})^{0.5}} \tag{3}$$

where A is the sensitive area of the photodetector, e is the electron charge, and I$_d$ is the dark current at a certain bias voltage. As shown in Table 2, the detectivity of the Fe$_3$O$_4$@TiO$_2$/Si was higher than that of the Fe$_3$O$_4$/Si photodetector, which means that the Fe$_3$O$_4$@TiO$_2$/Si can be used effectively to detect weak light signals. A comparison of the figures of merit of the fabricated Fe$_3$O$_4$@TiO$_2$/Si photodetector with other heterojunction-based silicon photodetectors of core–shell structure is found in Table 3.

4 Conclusion

We have demonstrated a novel route to synthesizing populated Fe$_3$O$_4$@TiO$_2$ core–shell/Si photodetector with a quantum efficiency higher than 100% at 400 nm without using a catalyst. Laser ablation of Fe$_3$O$_4$ in a solution of TiO$_2$ nanoparticles resulted in the production of a populated Fe$_3$O$_4$@TiO$_2$ core–shell structure. The structural and optical properties of Fe$_3$O$_4$ nanoparticles and Fe$_3$O$_4$@TiO$_2$ core–shell nanoparticles were investigated. XRD data confirmed the formation of crystalline Fe$_3$O$_4$@TiO$_2$. TEM studies suggest the presence of Fe$_3$O$_4$@TiO$_2$ core–shell nanoparticles with an average particle size of 60 nm. The optical energy gap of core–shell was larger than that of magnetite. The junction characteristics of the Fe$_3$O$_4$@TiO$_2$ core–shell/Si are better than those of Fe$_3$O$_4$/Si. The responsivity of the Fe$_3$O$_4$@TiO$_2$ core–shell/Si photodetector was 0.5A/W at 400 nm, while the responsivity of Fe$_3$O$_4$/Si was 0.4A/W at 500 nm. The external quantum efficiency and specific detectivity of the Fe$_3$O$_4$@TiO$_2$ core–shell/Si were higher than those of Fe$_3$O$_4$/Si. The technique used for core–shell is competitive, inexpensive, and suitable for the fabrication of high-performance photodetectors.

a responsivity of 0.5A/W, while the Fe$_3$O$_4$/Si photodetector has a peak response at 475 nm with a responsivity of 0.4A/W. This blue shift can be explained on the basis that the energy gap of Fe$_3$O$_4$@TiO$_2$ core–shell is larger than that of Fe$_3$O$_4$ NPs. As is obvious from Fig. 9, the Fe$_3$O$_4$@TiO$_2$ core–shell/Si photodetector has a quantum efficiency greater than 100% in the spectral region (400-550 nm), while the Fe$_3$O$_4$/Si photodetector has a quantum efficiency of less than 100%.

This improvement can be ascribed to the presence of core–shell structure, which contributes significantly to the decrease in the e–h recombination as a result of the presence of a high electric field. Table 2 lists the specific detectivity (D*) and the noise equivalent power (NEP) of

Table 3 A Comparison between the Figs. of merit of various Si-based core–shell photodetectors with Fe_3O_4@TiO_2/Si

Photodetector type	Responsivity (A/W)	D* (Jones)	EQE%
p-Si/n-InP [37]	2.74 at 920 nm	5.52×10^{11} at 920 nm	–
CuO@CuS/Si [38]	0.79	8.11×10^{11}	3.09×10^2
Au@PbI_2/Si [39]	0.39 at 800 nm	4×10^{12} at 800 nm	6.04 at 800
Fe_3O_4@TiO_2/Si [Current work]	0.5 at 400 nm	1.9×10^{11} at 400 nm	1.5×0^2 at 400 nm

References

1. S. Shen, L. Wu, M. Xie, H. Shen, Core shell structured Fe_3O_4@TiO_2 doxorubicin nanoparticles for targeted chemo-sonodynamic therapy of cancer. Int. J. Pharm. **486**, 380–388 (2015)

2. Y. Chen, Y. Gao, Y. Li, Synergistic chemo-photodynamic therapy mediated by light-activated ROS-degradable nanocarriers. J. Mater. Chem. B **7**, 460 (2019)

3. V. Kharissova, B. Kharisov, C. González, Greener synthesis of chemical compounds and materials. R. Soc. Open. Sci. **11**, 191378 (2019)

4. G. Amoabediny, A. Naderi, J. Malakootikhah, Guidelines for safe handling, use and disposal of nanoparticles. J. Phys.: Conf. Ser. **170**, 012037 (2009)

5. A. Priya, A. Sunny, B. Karthikeyan, D. Sastikumar, Optical, spectroscopic and fiber optic gas sensing of potassium doped α-Fe_2O_3 nanostructures, author links open overlay panel. Opt. Fiber Technol. **58**, 102304 (2020)

6. S. Rao, A. Priya, S. Kamath et al., Unequivocal evidence of enhanced room temperature sensing properties of clad modified Nd doped mullite $Bi_2Fe_4O_9$ in fiber optic gas sensor. J. Alloys Comp. **838**, 155603 (2020)

7. G. Yuxiang, G. Cao, X. Li, Single-nanowire silicon photodetectors with core-shell radial Schottky junction for self-powering application. Appl. Phys. Lett. **118**, 153904 (2021)

8. M. Mozafari, Sh. Nasresfahani, M. Sheikhi, H. Agharezaei, An enhanced Vis-NIR photodetector based on Ag@ PbS core-shell plasmonic heterostructure. J. Alloys Comp. **850**, 156831 (2021)

9. R. Ismail, R. Abdul-Hamed, Laser ablation of Au–CuO core–shell nanocomposite in water for optoelectronic devices. Mater. Res. Expr. **4**, 125020 (2017)

10. R. Ismail, A. Mousa, M. Amin, Synthesis of hybrid Au@ PbI_2 core-shell nanoparticles by pulsed laser ablation in ethanol. Mater. Res. Expr. **11**, 115024 (2018)

11. Y. Li, J. Wu, D. Qi et al., Novel approach for the synthesis of Fe_3O_4@TiO_2 core–shell microspheres and their application to the highly specific capture of phosphopeptides for MALDI-TOF MS analysis. Chem. Commun. **5**, 564–566 (2008)

12. W. Chen, P. Tsai, Y. Chen, Functional Fe_3O_4/TiO_2 core/shell magnetic nanoparticles as photokilling agents for pathogenic bacteria. Small **4**, 485–491 (2008)

13. Y. Li, J. Wu, D. Qi et al., Novel approach for the synthesis of Fe_3O_4@ TiO_2 core–shell microspheres and their application to the highly specific capture of phosphopeptides for MALDI-TOF MS analysis. Chem. Commun. **5**, 564–566 (2008)

14. T. Sasaki, Y. Shimizu, N. Koshizaki, Preparation of metal oxide-based nanomaterials using nanosecond pulsed laser ablation in liquids. J. Photochem. Photobiol., A **182**, 335–341 (2006)

15. A. Priya, K. Yogesh, K. Subha et al., Synthesis of silver nano-butterfly park by using laser ablation of aqueous salt for gas sensing application. Appl. Phys. A **127**, 292 (2021)

16. A. Priya, D. Sastikumar, Nano-second pulsed laser ablation and transformation of bulk titanium dioxide (TiO_2) into nano-particles for fiber optic gas sensor AIP Conference Proceedings 2265, 030169 (2020); https://doi.org/10.1063/5.0017169

17. G. Yogesh, E. Shuaib, A. Priya et al., Synthesis of water-soluble fluorescent carbon nanoparticles (CNPs) from nanosecond pulsed laser ablation in ethanol. Opt. Laser Technol. **135**, 106717 (2021)

18. A. Priya, Subha K. Raoa, G. Yogesh,P. Rohini , D. Sastikumar, Green synthesis of Silver Nanoparticles by Pulsed Laser ablation using Citrus Limetta juice extract for Clad-Modified Fiber Optic gas sensing application, Proceedings Volume 11802, Nanoengineering: Fabrication, Properties, Optics, Thin Films, and Devices XVIII; 1180214 (2021) SPIE Nanoscience + Engineering, 2021, San Diego, California, United States

19. L. Finger, R. Hazen, A. Hofmeister, High-pressure crystal chemistry of spinel ($MgAl_2O_4$) and magnetite (Fe_3O_4): comparisons with silicate spinels. Phys. Chem. Miner. **13**, 215–220 (1986)

20. G.D. ShiraneCox, W. Takei, S. Ruby, A study of the magnetic properties of the $FeTiO_3$-αFe_2O_3 system by neutron diffraction and the Mössbauer effect. J. Phys. Soc. Jpn. **17**(10), 1598–1611 (1962)

21. E. Meagher, G. Lager, Polyhedral thermal expansion in the TiO_2 polymorphs; refinement of the crystal structures of rutile and brookite at high temperature. Can. Mineral. **1**, 77–85 (1979)

22. R. Ismail, S. Zaidan, R. Kadhim, Preparation and characterization of aluminum oxide nanoparticles by laser ablation in liquid as passivating and anti-reflection coating for silicon photodiodes. Appl. Nanosci. **7**, 477–487 (2017)

23. R. Ismail, G. Sulaiman, S. Abdulrahman, Preparation of iron oxide nanoparticles by laser ablation in DMF under effect of external magnetic field. Int. J. Mod. Phys. B **30**(17), 1650094 (2016)

24. J. Lalatonne, Y. Richardi, M. Pileni, Van der Waals versus dipolar forces controlling mesoscopic organizations of magnetic nanocrystals. Nat. Mater. **3**, 121–125 (2004)

25. R. Ismail, G. Sulaiman, M. Mohsin, A. Saadoon, Preparation of silver iodide nanoparticles using laser ablation in liquid for antibacterial applications. IET Nanobiotechnol. **12**, 781–786 (2018)

26. T. Iwamoto, T. Ishigaki, Fabrication of iron oxide nanoparticles using laser ablation in liquids. J. Phys.: Conf. Ser. **441**, 012034 (2013)

27. F. Weigert, A. Müller, I. Häusler et al., Combining HR-TEM and XPS to elucidate the core–shell structure of ultrabright CdSe/CdS semiconductor quantum dots. Sci. Rep. **10**, 20712 (2020)

28. V. Tkachenko, L. Vidal, L. Josien et al., Characterizing the core-shell architecture of block copolymer nanoparticles with electron microscopy: a multi-technique approach. Polymers **12**, 1656 (2020)

29. M. Kumar, P. Chamoli, K. Kar, Enhanced photocatalytic degradation of methylene blue and adsorption of arsenic (iii) by reduced graphene oxide (rGO)–metal oxide (TiO_2/Fe_3O_4) based nanocomposites. RSC Adv. **5**, 73249–73260 (2015)

30. R. Verma, J. Gangwar, A. Srivastava, Multiphase TiO_2 nanostructures: a review of efficient synthesis, growth mechanism, probing capabilities, and applications in bio-safety and health. RSC Adv. **7**, 44199–44224 (2017)

31. T. Szatkowski, M. Wysokowski, G. Lota et al., Novel nanostructured hematite–spongin composite developed using an extreme biomimetic approach. RSC Adv. **5**, 79031–79040 (2015)

32. R. Ismail, K. Khashan, M. Jawad, A. Mousa, F. Mahdi, Preparation of low cost n-ZnO/MgO/p-Si heterojunction photodetector by laser ablation in liquid and spray pyrolysis. Mater. Res. Expr. **5**, 055018 (2018)

33. R. Ismail, Improved characteristics of sprayed CdO films by rapid thermal annealing. J. Mater. Sci.: Mater Electron **20**, 1219–1224 (2009)

34. R. Ismail, K. Hassan, O. Abdulrazaq, W. Abode, Optoelectronic properties of CdTe/Si heterojunction prepared by pulsed Nd: YAG-laser deposition technique. Mater. Sci. Semicond. Process. **10**, 19–23 (2007)

35. E. Salim, R. Ismail, M. Fakhri, B. Rasheed, Z. Salim, Synthesis of cadmium oxide/Si heterostructure for two-band sensor application. Iran J. Sci. Technol. Trans. Sci. **43**, 1337–1343 (2019)

36. S. Das, K. Sarkar, B. Pal, SnS$_2$/Si nanowire vertical heterostructure for high performance ultra-low power broadband photodetector with excellent detectivity. J. Appl. Phys. **129**, 053105 (2021)

37. B. Pal, K. Sarkar, S. Das, P. Banerji, Near-infrared detection in Si/InP core-shell radial heterojunction nanowire arrays. J. Alloys Comp. **885**, 160943 (2021)

38. S. Gunasekaran, D. Thangaraju, R. Marnadu et al., Photosensitive activity of fabricated core-shell composite nanostructured p-CuO@CuS/n-Si diode for photodetection applications. Sensors Actuat. A: Phys. **317**, 112373 (2021)

39. A.M. Mousa, R.A. Ismail, M.H. Amin, Hybrid p-Au@PbI$_2$/n-Si heterojunction photodetector prepared by pulsed laser ablation in liquid. Opt. – Int. J. Light Electron Opt. **183**, 933–941 (2019)